Quasiparticle dynamics in graphene

AARON BOSTWICK[1], TAISUKE OHTA[1,2], THOMAS SEYLLER[3], KARSTEN HORN[2] AND ELI ROTENBERG[1]*

[1] Advanced Light Source, E. O. Lawrence Berkeley National Laboratory, Berkeley, California 94720, USA
[2] Department of Molecular Physics, Fritz-Haber-Institut der Max-Planck-Gesellschaft, Faradayweg 4-6, 14195 Berlin, Germany
[3] Institut für Physik der Kondensierten Materie, Lehrstuhl für Technische Physik, Universität Erlangen-Nürnberg, Erwin-Rommel-Straße 1, D-91058 Erlangen, Germany
*e-mail: erotenberg@lbl.gov

Published online: 10 December 2006; doi:10.1038/nphys477

The effectively massless, relativistic behaviour of graphene's charge carriers—known as Dirac fermions—is a result of its unique electronic structure, characterized by conical valence and conduction bands that meet at a single point in momentum space (at the Dirac crossing energy). The study of many-body interactions amongst the charge carriers in graphene and related systems such as carbon nanotubes, fullerenes and graphite is of interest owing to their contribution to superconductivity and other exotic ground states in these systems. Here we show, using angle-resolved photoemission spectroscopy, that electron–plasmon coupling plays an unusually strong role in renormalizing the bands around the Dirac crossing energy—analogous to mass renormalization by electron–boson coupling in ordinary metals. Our results show that electron–electron, electron–plasmon and electron–phonon coupling must be considered on an equal footing in attempts to understand the dynamics of quasiparticles in graphene and related systems.

With the recent discovery of superconductivity in carbon nanotubes[1,2], alkaline-metal-doped C_{60} crystals[3] and graphite intercalation compounds[4–6] with relatively high transition temperatures, there is a strong interest in the influence of many-body interactions on the electron dynamics in these systems. Graphene is a sheet of carbon atoms distributed in a honeycomb lattice and is the building block for all of these materials; therefore, it is a model system for this entire family. Recently, graphene has been isolated using exfoliation from graphite[7,8] and graphitization of SiC[9,10], enabling, for the first time, the direct measurement of the many-body interactions fundamental to all of these carbon systems. These interactions could be especially interesting owing to the effectively massless, relativistic nature of the charge carriers, which follows from the formal equivalence of the Schrödinger wave equation to the relativistic Dirac equation for graphene[7,8,11]. This equation leads to linear bands that cross at the Dirac energy E_D, which can be expressed in terms of angular frequency ω_D as $E_\mathrm{D} = \hbar\omega_\mathrm{D}$, where $\hbar$ is the reduced Planck constant.

The coupling among quasiparticles is fundamental to understanding superconductivity and other exotic ground states. We focus in particular on the interaction of the carriers with electron–hole pair excitations within the Fermi-liquid model, and with plasmons. Departure of the electron dynamics from Fermi-liquid behaviour in graphite has already been attributed to the special shape of the graphene band structure[12,13], whereas electron–plasmon scattering has been proposed as a key coupling process in superconductivity[14] of cuprates[15], and possibly metallized graphene[16]. Angle-resolved photoemission spectroscopy (ARPES) probes the scattering rate at different energy scales, and therefore accesses these many-body couplings directly. We find that both electron–hole and electron–plasmon effects are important for graphene, depending on the energy scale, and, together with electron–phonon coupling, are necessary for a complete picture of the quasiparticle dynamics.

The single-particle graphene band structure $E(\mathbf{k})$ may be described by a simple one-orbital tight-binding model as[17]

$$E(\mathbf{k}) = \pm t\sqrt{1+4\cos(\sqrt{3}ak_y/2)\cos(ak_x/2)+4\cos^2(ak_x/2)} \tag{1}$$

where $\mathbf{k}$ is the in-plane momentum, a is the lattice constant and t is the near-neighbour hopping energy. That the carriers travel as effectively massless particles with a fixed 'speed of light' $c^* = \hbar^{-1}\mathrm{d}E(k)/\mathrm{d}k \sim c/300$, follows from the nearly linear dispersion of the bands at zero energy (E_D). In Fig. 1 we compare energy bands and constant-energy surfaces computed using equation (1) with the first (to our knowledge) ARPES measurements applied to a single layer of graphene, grown on the (0001) surface of SiC (6H polytype). (Previous ARPES measurements near the Fermi energy E_F have focused on thicker graphene layers on SiC[18–20] or on bulk graphite[21,22].) The primary bands, cones centred at the K points, are surrounded by six weak replica bands discussed further below. The primary bands are in good overall agreement with the simple model despite it having only two adjustable parameters: the hopping energy $t = 2.82$ eV and a 0.45 eV shift of E_F above the Dirac crossing energy E_D. This shift is attributed to doping of the graphene layer by depletion of electrons from the n-type SiC.

We can discriminate a single layer of graphene from thicker films by counting the number of π-states (one in Fig. 1), which is equal to the number of layers m in a given sample[20]. Whereas films of thickness $m \geq 2$ often coexist with $(m \pm 1)$-layer domains, we found that pure graphene films $(m = 1)$ can be routinely isolated. We can also be sure that there is negligible interaction between overlayer and substrate states. This follows naturally from the fact that the Fermi level of the graphene is pinned well within the $\sim$3 eV bandgap of the substrate. If there was hybridization with the substrate, we would expect it not near E_F but rather at a deeper binding energy, where the substrate and graphene bands

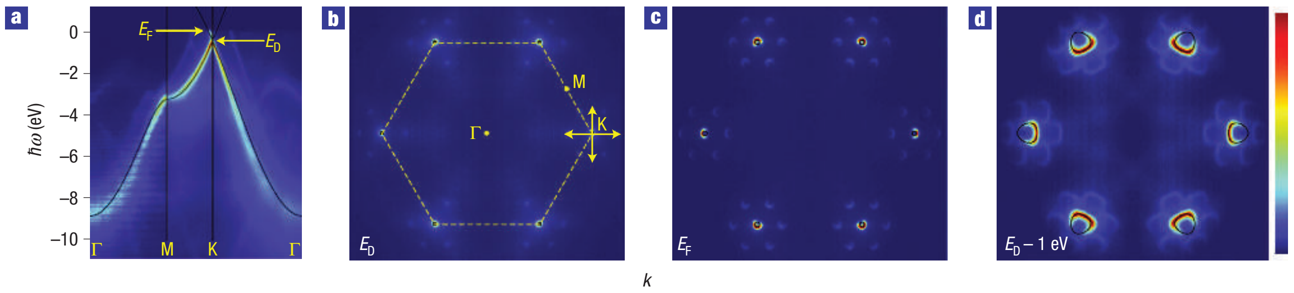

Figure 1 The band structure of graphene. a, The experimental energy distribution of states as a function of momentum along principal directions, together with a single-orbital model (solid lines) given by equation (1). **b**, Constant-energy map of the states at binding energy corresponding to E_D together with the Brillouin zone boundary (dashed line). The orthogonal double arrows indicate the two directions over which the data in Fig. 2 were acquired. **c**,**d**, Constant-energy maps at $E_F (= E_D + 0.45)$ (**c**) and $E_D - 1$ eV (**d**). The faint replica bands correspond to the $6\sqrt{3} \times 6\sqrt{3}$ satellite peaks in low-energy electron diffraction[9].

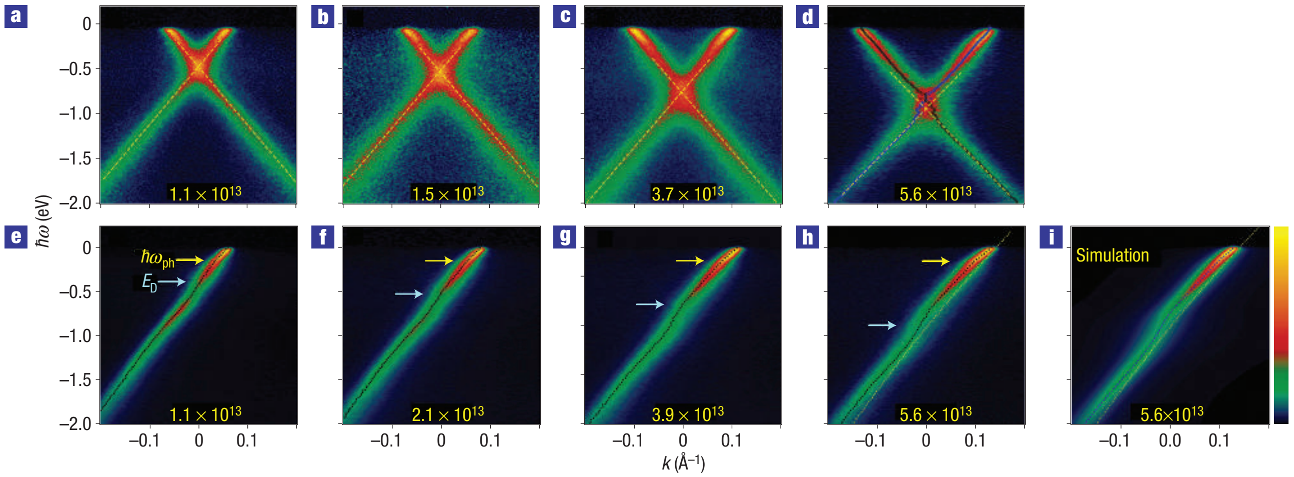

Figure 2 The band structure of graphene near the Fermi level. a–d, Experimental energy bands along a line through the K point parallel to the ΓM direction (along the vertical double arrow in Fig. 1b) as a function of progressively increased doping by potassium adsorption. The dashed lines are an extrapolation of the lower bands (below E_D), which are observed not to pass through the upper bands (above E_D), suggesting the kinked shape of the bands around E_D. The electron density (per cm^2) is indicated in each panel. **e–h**, Band maps for similar dopings acquired in an orthogonal direction through the K point (horizontal double arrow in Fig. 1b), for which one of the bands is suppressed. The nonlinear, or 'kinked', dispersion of the bands together with linewidth variations (corresponding to real and imaginary parts of the self-energy Σ) are clearly visible in the fitted peak positions (dotted lines). The kinks, marked by arrows, occur at a fixed energy of 200 meV and near E_D, the latter varying with doping. **i**, The simulated spectral function, calculated using only the bare band (yellow dotted line) and Im Σ derived from the data in panel **h**.

overlap. Even there, we see no indication of interactions between the graphene and substrate band structures in Fig. 1.

Such interactions are not expected considering the proposed van der Waals bonding between graphene and SiC (ref. 9). Recent experiments have shown that the SiC layer immediately below the graphene is itself a carbon-rich layer, with an in-plane, graphene-like network of sp^2-derived σ-bands, but without graphene-like π-bands[23]. The absence of states at the Fermi level suggests that the p_z orbitals are saturated, presumably owing to bonding with the substrate as well as bonding within the C-rich interface layer. This C-rich layer is a perfect template for van der Waals bonding to the overlying graphene because it offers no p_z orbitals for bonding to the graphene. The photon-energy dependence of the π-band intensities, absent for $m = 1$ films, but clearly observed for $m \geq 2$, confirms this lack of hybridization (T.O., A.B., J.L.McC., T.S., K.H., E.R., manuscript in preparation).

The only effect of the interface on the measurements is through the nearly incommensurate $(6\sqrt{3} \times 6\sqrt{3})R30^\circ$ symmetry of the interface C-rich layer with respect to SiC. This interface induces diffraction of the primary bands, resulting in the observed weak satellite bands, similar to the satellite spots seen in low-energy electron diffraction[9].

Despite the overall good agreement between equation (1) and the data in Fig. 1, profound deviations are observed when we examine the region around E_F and E_D in more detail. Figure 2a shows a magnified view of the bands measured along a line (the vertical double arrow in Fig. 1b) through the K point. The predicted, or 'bare' bands in this direction are nearly perfectly linear and mirror symmetric with respect to the K point according to equation (1), similar to the H point of bulk graphite[21,22]. The actual bands deviate from this prediction in two significant ways. First, at a binding energy $\hbar\omega_{ph} \sim 200$ meV below E_F, we observe a sharpening of the bands accompanied by a slight kink in the bands' dispersions. We attribute this feature to renormalization of the electron bands near E_F by coupling to phonons[24], as discussed later.

Second, and more surprisingly, linear extrapolations of the lower bands (dashed lines in Fig. 2a) do not pass through the upper bands, demonstrating that the bands do not pass smoothly through E_D as equation (1) predicts. This is observed more easily for data acquired along the orthogonal direction through the K point (Fig. 2e), along which an interference effect[25] suppresses one of the two bands. We see that near E_D the bands have an additional kink, which we propose is caused by other many-body interactions.

The deviations from the bare band are sensitive to doping, which was varied by adsorbing potassium atoms that readily donate electrons to the graphene. The evolution of the band structure with increasing doping is followed in Fig. 2b–d and along the orthogonal direction in Fig. 2f–h. Similar to graphite, doping graphene by K deposition shifts the bands more or less rigidly to higher binding energy[26]. Whereas the energy of the kink at 200 meV does not change, the deeper-energy kink strengthens and follows E_D with doping, demonstrating that it is associated with electrons with energy near E_D. The effect of this kink on the band structure is significant: at high doping, a curve fit of the band positions (small circles in Fig. 2d) shows that E_D has been shifted towards E_F by ∼130 meV from the single-particle prediction.

In the quasiparticle scheme, the carriers are represented as single particles that scatter from, and are surrounded by, a cloud of other 'particles' (such as phonons); the entire entity moves rather like a free particle but with renormalized energy. In this scheme, ARPES measures the spectral function, expressed in terms of the complex self-energy $\Sigma(\mathbf{k},\omega)$, as

$$A(\mathbf{k},\omega)=\frac{|\mathrm{Im}\,\Sigma(\mathbf{k},\omega)|}{(\omega-\omega_b(\mathbf{k})-\mathrm{Re}\,\Sigma(\mathbf{k},\omega))^2+(\mathrm{Im}\,\Sigma(\mathbf{k},\omega))^2}$$

where ω is the energy and ω_b is the bare band dispersion in the absence of many-body effects. $\Sigma(\mathbf{k},\omega)$ contains both the scattering rate and the renormalization of the band dispersion in its imaginary and real parts, respectively. In the **k**-independent approximation[27,28] ($\Sigma(\mathbf{k},\omega)\approx\Sigma(\omega)$), Im $\Sigma(\omega)$ is proportional to the Lorentzian linewidth of the momentum distribution curve (MDC) $A(\mathbf{k},\omega)$ taken at constant ω. Re $\Sigma(\omega)$ is readily computed from Im $\Sigma(\omega)$ through a Hilbert transform (to satisfy causality), and the full spectral function $A(\mathbf{k},\omega)$ can be reconstructed using the computed Re $\Sigma(\omega)$ and compared with experiment. Such a reconstruction for one doping is shown in Fig. 2i; it is in excellent agreement with the data (Fig. 2h) from which Im Σ was obtained. This shows that all the kinks in the bands originate not from details of the single-particle band structure, but rather from many-body interactions, providing strong support for the quasiparticle picture in graphene.

The observed kink structure is therefore derived from a complicated ω-dependence of the observed scattering rate proportional to the measured MDC linewidths, shown in Fig. 3 as a function of doping. To model these data, we consider three processes: decay of the carriers by electron–phonon (e–ph) coupling, by electron–hole (e–h) pair generation and by emission of collective charge excitations (plasmons) via electron–plasmon (e–pl) coupling. (Impurity scattering, a fourth contributing process, can be ignored, as its contribution to the MDC linewidth is smaller than the experimental momentum resolution (∼0.01 Å^{-1}) and in any case merely leads to a uniform background scattering rate.) By summing all the momentum- and energy-conserving decay events as a function of hole energy ω, we can show that the three principal decay processes (e–h, e–pl, and e–ph) contribute differently to the lifetime in regions I–IV as identified in the traces in the upper part of Fig. 3, calculated for a sample with $n=5.6\times10^{13}$ cm^{-2}, and compares favourably with the experimental MDC width for this doping; we can also obtain similar agreement for the other dopings. (The predicted dip at E_D is an artefact of the simplicity of our model, which does not consider interactions between the plasmons and the Fermi-liquid excitations.)

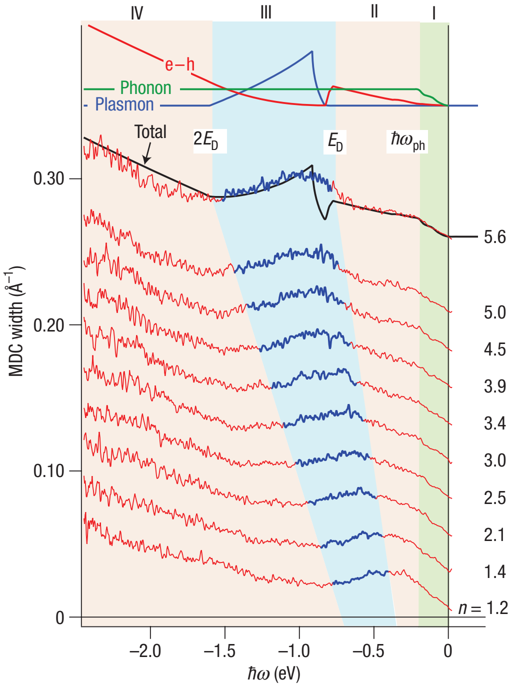

Figure 3 MDC widths of carriers in graphene. Measured spectral MDC width (assumed proportional to scattering rate and Im Σ) for graphene, derived by carrying out a line-shape analysis of MDC for each binding energy as a function of doping n (in units of 10^{13} cm^{-2}). Each trace is shifted upward by 0.025 Å^{-1}. The simulated total scattering rate (black line) and the partial contributions due to decay into phonons (green), electron–hole pairs (red) and plasmons (blue) are compared with the MDC spectral width for the highest doped sample. The plasmon calculation was for $\varepsilon=10$. These interactions contribute differently in regions I–IV defined as follows: (I) the phonon energy scale $\omega_{ph}<\omega<0$, (II) the Dirac energy scale $\omega_D<\omega<0$, (III) $2\omega_D<\omega<\omega_D$ and (IV) $\omega<2\omega_D$.

Now we discuss the different decay processes in turn. We attribute the kink near E_F to e–ph coupling as described previously for metals[29–31], for (possibly) high-T_c superconductors[32,33] and for bulk graphite[24]. In this process, photoholes decay by phonon emission (see Fig. 4a). From graphite's phonon density of states[34], we calculated the e–ph contribution to Im Σ (Fig. 3, green curve) with the standard formalism[35] and found an e–ph coupling constant $\lambda\approx0.3$. Although this is a factor of five larger than predicted[36] for $n=5.6\times10^{13}$ cm^{-2}, comparison with the experimental data shows that this provides an accurate description of Im Σ in region I. The observed increase of the kink's strength with n (see Fig. 2e–h) is expected from the increase in the size of the Fermi surface, although the 200 meV energy scale remains constant because the K atoms should not alter the phonon band structure at this energy.

Consider now the decay of the photohole by excitation of an electron from below to above E_F, thereby creating an e–h pair. In Landau's Fermi-liquid theory, the scattering rate from such processes increases as $\sim\omega^2$ away from $\omega=0$, reflecting the growing number of possible excitations that satisfy momentum and energy conservation. However, the linear dispersion of the graphene bands and the presence of the Dirac crossing below E_F drastically modify this picture[37]. A hole just above E_D can easily decay through many possible e–h creation events, for example, as in Fig. 4b, and we find

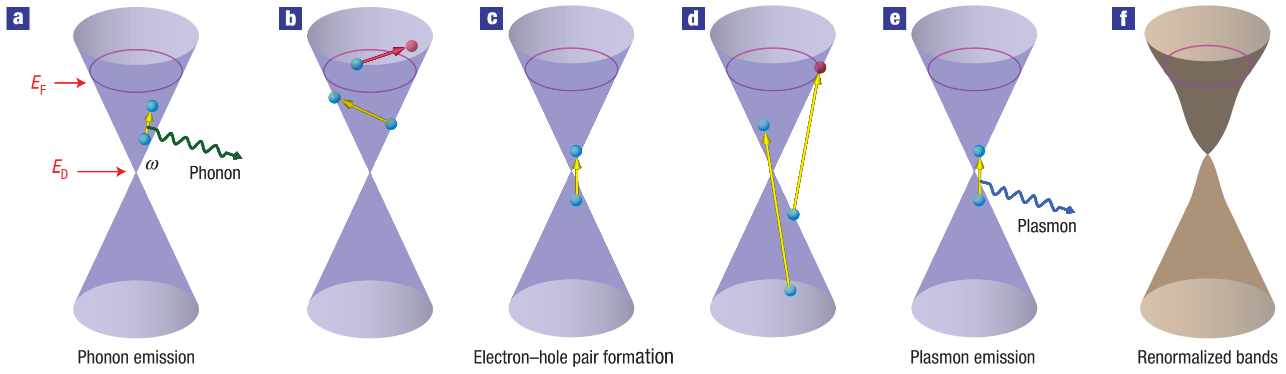

Phonon emission

Electron–hole pair formation

Plasmon emission

Renormalized bands

Figure 4 Decay processes in graphene. a, The energy–momentum diagram for decay processes of a photohole, initially created at energy ω, decaying by emission of a phonon. **b–d**, Spontaneous generation of an electron–hole pair near E_F for photohole energy satisfying $\omega > \omega_D$ (**b**), $2\omega_D < \omega < \omega_D$ (**c**), which can generate no possible e–h pair as drawn, and $\omega < 2\omega_D$ (**d**). **e**, Emission of a plasmon ($2\omega_D < \omega < \omega_D$). **f**, The net effect of these processes is to distort the bare bands to the renormalized bands (shown in brown).

a ω^α ($\alpha \sim 1.5$) dependence of $\mathrm{Im}\,\Sigma$ in regions I–II, in contrast with Fermi-liquid theory ($\alpha = 2$). However, a hole originating at ω just below E_D has few possible decays with sufficient momentum transfer to excite an e–h pair (Fig. 4c). This causes a sharp reduction in the scattering rate in region III, seen in the red curve in Fig. 3. Only for energies $\omega \lesssim 2\omega_D$, region IV, does e–h pair generation become favourable (for example, Fig. 4d).

The e–h and e–ph processes can explain the observed MDC widths in regions I, II and IV. In region III, however, decay by e–h pair creation is virtually not allowed, yet the observed scattering rate has a peak rather than a dip (highlighted in blue in Fig. 3). We now show that this peak may be explained by decay through plasmon emission. Plasmons are oscillations of an electron gas that play an important role in the optical properties of ordinary metals. In graphene, the charge carriers near the K point have zero effective mass and travel like photons at constant speed c^*, but unlike photons they have charge and are therefore subject to collective oscillations such as plasmons. Although a full treatment of the e–pl interaction is difficult near the Dirac point, a simple model suffices to explain how e–pl coupling can enhance the scattering rate below E_D.

Ordinary two-dimensional plasmons have a dispersion relationship

$$\omega_{\mathrm{pl}}(q) = \sqrt{4\pi n e^2 q / m(1+\varepsilon)}, \qquad (2)$$

where q is the plasmon momentum, e is the electron charge, m is the effective carrier mass and ε is the dielectric constant. For graphene, the rest mass m_0 is zero near E_D, but the 'relativistic mass' $m_r = E/c^{*2}$ depends on the doping[7,8], reaching a maximum of only 10% of the free-electron rest mass for our samples; this has the notable effect of increasing the plasmon energy $\omega_{\mathrm{pl}}(q)$, as shown in Fig. 5, calculated for a reasonable range ($3 < \varepsilon < 10$) of dielectric constants.

Collective plasmon excitations are not really independent of the e–h pair excitations discussed above, and therefore decay by plasmon scattering is a valid description only outside the range of kinematically allowed e–h processes, as shown in Fig. 5 for n-doped graphene. This only occurs for decay processes with $\omega \sim E_D$ and $q \sim 0$ (as in Fig. 4e), when the plasmon spectrum does not overlap the continuum of e–h excitations (blue region in Fig. 5). This means that plasmons can have a large effect on the self-energy around $\omega \sim \omega_D$.

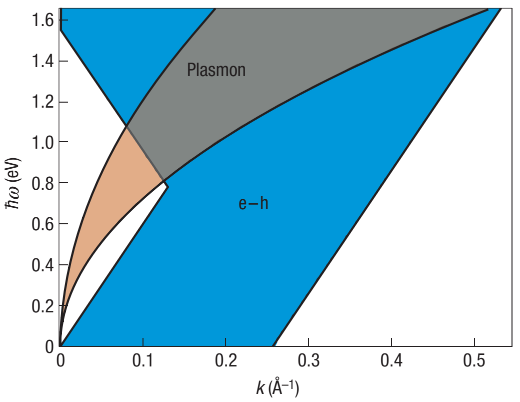

Figure 5 Energy diagram of electronic excitations in graphene. The blue region shows the possible e–h pair excitations for graphene, computed for a conical band structure with $n = 5.6 \times 10^{13}$ cm^{-2}, as in Fig. 4a. The pink region shows the plasmon dispersion calculated for a range of dielectric constants from $\varepsilon = 3$ (upper rim) to $\varepsilon = 10$ (lower rim) using equation (2) together with the relativistic mass taken from transport measurements[7,8]. The e–pl decay process occurs only for plasmons outside the blue region, where plasmons are well-defined quasiparticles.

Given the plasmon dispersion relation, we can easily sum the possible plasmon decays as a function of ω (Fig. 3, blue curve), which is proportional to the scattering rate. We find a peak in $\mathrm{Im}\,\Sigma$ located just below E_D, whose width and intensity scales with E_D. A peak following these trends is clearly observed in the experimental data (highlighted in blue in Fig. 3).

Previously, e–pl coupling was shown to affect the unoccupied bands of a three-dimensional metal at the large plasmon energy scale (~20 eV) (ref. 38), but e–pl coupling at small energy scales is normally forbidden for two- and three-dimensional electron gases (except for the special case of layered electron gases[39]), so this is a unique instance where e–pl coupling is kinematically allowed for a pure two-dimensional system.

It is worth emphasizing that the model for the scattering rate has only four adjustable scaling factors: the e–ph coupling constant λ, the absolute probabilities for e–h pair creation and plasmon emission and the screening constant ε, which scales the Coulomb interaction. The other inputs are the experimentally determined band dispersion, the graphite phonon density of states[34] and the relativistic mass[7,8] m_r.

These results show that the special condition of massless Dirac fermions found in graphene does not preclude the validity of the quasiparticle picture—in fact, the quasiparticle picture is valid over a spectacularly wide energy range—but it does induce novel e–h and e–pl decay processes. Thus, it is an exceptional combination of effects—the unusual band structure of graphene (leading to a large hole in the phase space for e–h pairs) together with the small effective mass of the carriers (leading to a plasmon spectrum that fills this hole)—that leads to these novel effects. These result in strong modifications of the band dispersion, as schematically shown in Fig. 4f. This distortion occurs not only near the Fermi level as in conventional metals, but also centred around the Dirac crossing energy E_D. The effects we describe are not unique to high doping levels, but extrapolate all the way down to zero doping. Near this regime (already approached for the lowest dopings in Fig. 3b), the energy scales for e–h, e–pl and e–ph decay processes overlap, and a unified treatment of all these interactions is necessary to reproduce the many-body effects. These conclusions might apply as well to graphite, which also shows a two-dimensional Dirac spectrum[40], metallic carbon nanotubes, which have a similar gapless band crossing[41] and Dirac fermions[42], and other materials with similar electronic structure[37].

METHODS

We conducted the ARPES measurements at the Electronic Structure Factory endstation at beamline 7.01 at the Advanced Light Source, equipped with a hemispherical Scienta R4000 electron analyser. We prepared the single layer of graphene by etching a 6H-SiC(0001) substrate (n-type with a nitrogen concentration of $(1.5\pm0.5)\times10^{18}$ cm^{-3} from SiCrystal AG) in hydrogen (pressure 1 bar, temperature 1,550 °C, time 30 min) followed by annealing at 1,150 °C for 4 min by direct current heating at pressure lower than 1×10^{-10} torr (refs 9,10). We conducted measurements at a pressure lower than 2.5×10^{-11} torr with the sample cooled to $\sim$20 K using a photon energy of 95 eV and with an overall energy resolution of $\sim$25 meV. Potassium deposition was by a commercial (SAES) getter source. We can estimate the potassium coverage from the carrier density assuming a charge transfer of $0.7e^-$ per alkali atom[43] to be about 0.007 monolayers when $n=1\times10^{13}$ cm^{-2}.

The range of dielectric constants ($3<\varepsilon<10$) used in the model is a rough estimate on the basis of dielectric constants of graphite (14), silicon carbide (10) and the vacuum (1).

Received 20 June 2006; accepted 1 November 2006; published 10 December 2006.

References

1. Tang, Z. K. *et al.* Superconductivity in 4 Angstrom single-walled carbon nanotubes. *Science* **292**, 2462–2465 (2001).
2. Kociak, M. *et al.* Superconductivity in ropes of single-walled carbon nanotubes. *Phys. Rev. Lett.* **86**, 2416–2419 (2001).
3. Hebard, A. F. *et al.* Superconductivity at 18 K in potassium-doped C60. *Nature* **350**, 600–601 (1991).
4. Hannay, N. B. *et al.* Superconductivity in graphitic compounds. *Phys. Rev. Lett.* **14**, 225–226 (1965).
5. Weller, T. E., Ellerby, M., Saxena, S. S., Smith, R. P. & Skipper, N. T. Superconductivity in the intercalated graphite compounds C$_6$Yb and C$_6$Ca. *Nature Phys.* **1**, 39–41 (2005).
6. Emery, N. *et al.* Superconductivity of bulk CaC$_6$. *Phys. Rev. Lett.* **95**, 087003 (2005).
7. Novoselov, K. S. *et al.* Two-dimensional gas of massless Dirac fermions in graphene. *Nature* **438**, 192–200 (2005).
8. Zhang, Y., Tan, Y. W., Stormer, H. L. & Kim, P. Experimental observation of the quantum Hall effect and Berry's phase in graphene. *Nature* **438**, 201–204 (2005).
9. Forbeaux, I., Themlin, J. M. & Debever, J. M. Heteroepitaxial graphite on 6H-SiC(0001): Interface formation through conduction-band electronic structure. *Phys. Rev. B* **58**, 16396–16406 (1998).
10. Berger, C. *et al.* Electronic confinement and coherence in patterned epitaxial graphene. *Science* **312**, 1191–1196 (2006).
11. DiVincenzo, D. P. & Mele, E. J. Self-consistent effective-mass theory for intralayer screening in graphite intercalation compounds. *Phys. Rev. B* **29**, 1685–1694 (1984).
12. Xu, S. M. *et al.* Energy dependence of electron lifetime in graphite observed with femtosecond photoemission spectroscopy. *Phys. Rev. Lett.* **76**, 483–486 (1996).
13. Moos, G., Gahl, C., Fasel, F., Wolf, M. & Hertel, T. Anisotropy of quasiparticle lifetimes and the role of disorder in graphite from ultrafast time-resolved photoemission spectroscopy. *Phys. Rev. Lett.* **87**, 267402 (2001).
14. Fröhlich, H. Superconductivity in metals with incomplete inner shells. *J. Phys. C Solid State Phys.* **1**, 544–548 (1968).
15. Ruvalds, J. Plasmons and high-temperature superconductivity in alloys of copper oxides. *Phys. Rev. B* **35**, 8869–8872 (1987).
16. Uchoa, B. & Castro Neto, A. Superconductivity in metal coated graphene. Preprint at <http://arxiv.org/abs/cond-mat/060815> (2006).
17. Wallace, P. R. The band theory of graphite. *Phys. Rev.* **71**, 622–634 (1947).
18. Strocov, V. N. *et al.* Photoemission from graphite: Intrinsic and self-energy effects. *Phys. Rev. B* **64**, 075105 (2001).
19. Rollings, E. *et al.* Synthesis and characterization of atomically thin graphite films on a silicon carbide substrate. *J. Phys. Chem. Solids* **67**, 2172–2177 (2006).
20. Ohta, T., Bostwick, A., Seyller, T., Horn, K. & Rotenberg, E. Controlling the electronic structure of bilayer graphene. *Science* **313**, 951–954 (2006).
21. Sugawara, K., Sato, T., Souma, S., Takahashi, T. & Suematsu, H. Fermi surface and edge-localized states in graphite studied by high-resolution angle-resolved photoemission spectroscopy. *Phys. Rev. B* **73**, 045124 (2006).
22. Zhou, S. Y. *et al.* First direct observation of Dirac fermions in graphite. *Nature Phys.* **2**, 595–599 (2006).
23. Emtsev, K. *et al.* Initial stages of the graphite-SiC(0001) interface formation studied by photoelectron spectroscopy. Preprint at <http://arxiv.org/abs/cond-mat/0609383> (2006).
24. Zhou, S. Y., Gweon, G. H. & Lanzara, A. Low energy excitations in graphite: the role of dimensionality and lattice defects. *Ann. Phys.* **321**, 1730–1746 (2006).
25. Shirley, E., Terminello, L., Santoni, A. & Himpsel, F. J. Brillouin-zone-selection effects in graphite photoelectron angular distributions. *Phys. Rev. B* **51**, 13614–13622 (1995).
26. Bennich, P. *et al.* Photoemission study of K on graphite. *Phys. Rev. B* **59**, 8292–8304 (1999).
27. Kaminski, A. & Fretwell, H. M. On the extraction of the self-energy from angle-resolved photoemission spectroscopy. *New J. Phys.* **7**, 98 (2005).
28. Kordyuk, A. A. *et al.* Bare electron dispersion from experiment: Self-consistent self-energy analysis of photoemission data. *Phys. Rev. B* **71**, 214513 (2005).
29. Valla, T., Fedorov, A. V., Johnson, P. D. & Hulbert, S. L. Many-body effects in angle-resolved photoemission: quasiparticle energy and lifetime of a Mo(110) suface state. *Phys. Rev. Lett.* **83**, 2085–2088 (1999).
30. Hengsberger, M., Purdie, D., Segovia, P., Garnier, M. & Baer, Y. Photoemission study of a strongly coupled electron-phonon system. *Phys. Rev. Lett.* **83**, 592–595 (1999).
31. Rotenberg, E., Schaefer, J. & Kevan, S. D. Coupling between adsorbate vibrations and an electronic surface state. *Phys. Rev. Lett.* **84**, 2925–2928 (2000).
32. Valla, T. *et al.* Evidence for quantum critical behavior in the optimally doped cuprate Bi$_2$Sr$_2$CaCu$_2$O$_{8+\delta}$. *Science* **285**, 2110–2113 (1999).
33. Lanzara, A. *et al.* Evidence for ubiquitous strong electron-phonon coupling in high-temperature superconductors. 412, 510–514 (2001).
34. Vitali, L., Schneider, M. A., Kern, K., Wirtz, L. & Rubio, A. Phonon and plasmon excitation in inelastic electron tunneling spectroscopy of graphite. *Phys. Rev. B* **69**, 121414 (2004).
35. Grimvall, G. *The Electron-Phonon Interaction in Metals* (North Holland, Amsterdam, 1981).
36. Calandra, M. & Mauri, F. Theoretical explanation of superconductivity in C$_6$Ca. *Phys. Rev. Lett.* **95**, 237002 (2005).
37. Castro Neto, A. Charge density wave, superconductivity, and anomalous metallic behavior in 2D transition metal dichalcogenides. *Phys. Rev. Lett.* **86**, 4382–4385 (2001).
38. Jensen, E., Bartynski, R. A., Gustafsson, T. & Plummer, E. W. Distortion of an unoccupied band in Be by the electron-plasmon interaction. *Phys. Rev. Lett.* **52**, 2172–2175 (1984).
39. Hawrylak, P. Effective mass and lifetime of electrons in a layered electron gas. *Phys. Rev. Lett.* **59**, 485–488 (1987).
40. Luk'yanchuk, I. & Kopelevich, Y. Phase analysis of quantum oscillations in graphite. *Phys. Rev. Lett.* **93**, 166402 (2004).
41. Hamada, N., Sawada, S. & Oshiyama, A. New one-dimensional conductors: Graphitic microtubules. *Phys. Rev. Lett.* **68**, 1579–1581 (1992).
42. Ando, T., Nakanishi, T. & Saito, R. Berry's phase and absence of back scattering in carbon nanotubes. *J. Phys. Soc. Jpn* **67**, 2857–2862 (1998).
43. Li, Z. Y., Hock, K. M., Palmer, R. E. & Annett, J. F. Potassium-adsorption-induced plasmon frequency shift in graphite. *J. Phys. Condens. Matter* **3**, S103–S106 (1991).

Acknowledgements

This work and the ALS were supported by the US Department of Energy, Office of Basic Sciences. K.H. and T.O. were supported by the Max Planck Society. We are grateful to J. L. McChesney for discussions and assistance with the experiments.
Correspondence and requests for materials should be addressed to E.R.

Author contributions

T.S. and K.H. prepared the SiC substrates. T.O. optimized the graphene quality with help from A.B.; A.B. and T.O. contributed equally to the graphitization during data runs and ARPES measurements. A.B. carried out theoretical modelling. E.R. carried out numerical analysis of the data. E.R. and A.B. wrote the text with review and input from all other co-authors.

Competing financial interests

The authors declare that they have no competing financial interests.